

Multi-Phase-Field Model Of Intergranular Corrosion Kinetics In Sensitized Metallic Materials

Talha Qasim Ansari ^{1,2}, Jing-Li Luo ² and San-Qiang Shi ^{1,z}

¹Department of Mechanical Engineering, the Hong Kong Polytechnic University, 11 Yuk Choi Road, Hung Hom, Kowloon, Hong Kong

²Department of Chemical and Materials Engineering, University of Alberta, Edmonton, AB, T6G1H9, Canada

^zCorresponding author Email: mmsqshi@polyu.edu.hk

Abstract

Improperly heat-treated metals exhibit preferential corrosion along sensitized grain boundaries when exposed to a corrosive electrolyte. This localized corrosion process is commonly known as Intergranular Corrosion (IGC). A multi-phase-field (MPF) model is presented to quantitatively predict IGC kinetics in metallic materials. The total free energy of the system is defined in terms of chemical, gradient and electromigration energy. The system is defined by a set of phase field variables which evolve due to the minimization of Gibbs free energy of the system. The simulation results show that IGC predicted by two-dimensional MPF model agrees well with the experimental results. The model also predicts plane-direction-dependent IGC in rolled sheets, commonly observed in the experimental studies. It is also observed that the corrosion process becomes transport controlled even at lower values of applied potentials due to the saturation of the metal ions in the corroded

grain boundaries region. A three-dimensional study is also presented to show the practical applications of using this MPF model for complex three-dimensional geometries.

Keywords: Intergranular corrosion, Multi-phase-field model

INTRODUCTION

IGC is a form of localized corrosion in which metal preferentially corrodes along the sensitized grain boundaries (SGBs) that can lead to the accelerated failure of metallic structures. IGC is a common problem in many alloy systems, for examples aluminum alloys and stainless steels, when reactive impurities segregate or passivating elements such as chromium are depleted at the grain boundaries. In IGC, SGBs corrode at a faster rate as compared to the grain due to compositional differences between grain boundaries and the metal adjacent to the boundary. Crystallographic plane orientations and stored grain energy – related to the defect density in the grains, also play an important role in IGC kinetics. Therefore, it is important to develop a thermodynamically consistent theoretical model that has the ability to quantitatively predict IGC kinetics of real metallic materials by explicitly considering all important electrochemical reactions and microstructural effects.

In the last few decades, several studies are reported in literature to better understand IGC kinetics and develop materials that are less susceptible to IGC. Most of this literature consists of experimental studies on IGC in aluminum ¹⁻¹², magnesium ¹³⁻¹⁵ and steel ¹⁶⁻¹⁸ alloys. In aluminum alloys, magnesium inside grains diffuses towards GBs at elevated temperatures (60 °C to 180 °C) or sometimes even at room temperature and results in an anodic β -phase (Al_3Mg_2) formation ⁴. Aluminum alloys having Mg composition more than 3% are more susceptible to IGC even at low temperatures. The experimental studies suggest that IGC in Al alloys is a function of applied potential, degree of sensitization (DoS), exposure time and rolling direction of the metal sheet ^{1, 4}. Apart from these

parameters, it has been found that crystal orientation ⁹, grain structure ¹⁰ and grain stored energy ^{5,6} also affect IGC kinetics.

Several models have been presented on IGC prediction over the years. In an early effort, Zhang et. al. proposed a statistical model (a so-called brick-wall model) to predict the IGC damage on the basis of alloy microstructure ¹⁹. A similar statistical model is proposed by Lim et. al. where IGC depths obtained from experiments serve as the input data for depth distribution to predict IGC growth ⁴. Their model is limited to AA5083 alloy when exposed to a 0.6M NaCl solution. Later, this model was extended to a 3-D geometry by using the Monte-Carlo method ²⁰. These statistical models show good agreement with the experimental findings. Mizuno et. al. proposed a FEM model ²¹ based on their experimental findings ²² to predict IGC penetration rate. It is also a relatively simple model and cannot predict IGC evolution with time. All of these models cannot predict the kinetic evolution of corroding surface and hence ignore the role of mass transport that greatly affects the evolving geometry. These models are also limited to the dissolution of only SGBs while experimental studies show that grains dissolution is not negligible at higher applied potentials ¹.

The Cellular automata (CA) method was also used to model IGC. In CA models ^{23,24}, every cell describes one physical state (grain matrix, SGB, electrolyte or passive film) in the domain. The transition of a grain or a SGB cell to electrolyte depends on the defined probability. Therefore, a higher probability is assigned to SGB cells as compared to grain matrix cells to predict IGC. More recently, Jafarzadeh et. al. proposed a peridynamic (PD) model to predict IGC ²⁵. Their model considers the dissolution of both grain matrix and

GBs by introducing effective diffusivity parameters that govern the dissolution rate of these two phases. Their model ignored the electro-migration effect and hence ignored the role of ionic species in the electrolyte. The electro-migration effect might play a key role in IGC kinetics as well, which would be worth investigating. Although this model makes significant improvement to the existing IGC models but leaves room for improvement in order to better understand and predict the process more accurately.

Phase-field (PF) models have been used to study pitting²⁶⁻²⁸ and stress-assisted²⁹⁻³¹ corrosion. More recently, a multi-PF (MPF) model is reported that includes the evolution of insoluble corrosion product (ICP) and its effect on pitting corrosion kinetics^{32,33}. To the best of our knowledge, a model for IGC based on phase field formulation is yet to be developed. In this work, a MPF model is proposed to investigate IGC kinetics of sensitized alloys in a corrosive environment.

The paper is organized as follows. In the Model section, the MPF model derivation is detailed for the grain–SGB–electrolyte system by defining the Gibbs free energy of the system, which consists of chemical, migration and gradient free energy. The evolution of the order parameters is derived from rate theory. The evolution of ionic concentration is governed by the Nernst-Planck equation, which consists of diffusion, migration and reaction terms, while the electrostatic potential distribution is governed by the Poisson equation. In the Results and Discussion section, the proposed MPF model of IGC is solved numerically for 2-D and 3-D geometries. The results are quantitatively compared with several experimental and numerical modelling results and relevant discussions are made in detail.

MODEL

ELECTROCHEMICAL REACTIONS

In Al-Mg alloys, Mg diffuses towards the SGBs at elevated or even at ambient temperatures to form β -phase (Al_3Mg_2). This results in a local galvanic couple in which the element composition near the SGBs is significantly different than the grain matrix. The aluminum oxidation reaction is given by,



A sensitized metal can undergo IGC both with and without applied potential depending on the degree of the sensitization and the nature of the electrolyte. The schematic of the process is shown in Fig 1.

MULTI-PHASE-FIELD FORMULATION

A MPF formulation for IGC is detailed in this section. The driving force of the metal oxidation is due to the minimization of Gibbs free energy of the system, which consists of chemical (f_{chem}), gradient (f_{grad}) and electrostatic free energy (f_{elec}),

$$G = \int_V \left[f_{\text{chem}}(\eta_k, C_i) + f_{\text{grad}}(\eta_k) + f_{\text{elec}}(C_i, \varphi) \right] dV \quad (2)$$

where η_k represents the phase field variables for phase k , C_i is the molar concentration of the ionic specie i and φ describes the electrostatic potential in the electrolyte. In this study, salt (NaCl) water is used as an electrolyte where Cl^- molarity is varied accordingly (from 0.1 to 1 mol/L) to compare modeling results with the experimental studies. The chemical free energy density of the system can be defined as,

$$f_{chem} = f_0 + RT \sum_i C_i \ln C_i + \sum_i C_i \mu_i^\ominus \quad (3)$$

where f_0 is a Landau polynomial of fourth order expressed as,

$$f_0 = m \left[\sum_{k=1}^N \left(\frac{\eta_k^4}{4} - \frac{\eta_k^2}{2} \right) + \sum_k \sum_{j>k}^N \gamma_{k,j} \eta_k^2 \eta_j^2 + \frac{1}{4} \right] \quad (4)$$

where m and $\gamma_{k,j}$ are model parameters related to physical parameters, surface energy (σ_k) and width of the interface (l). The second term in Eq. (3) is the free energy of the electrolyte, where R and T are the gas constant and absolute temperature, respectively. The last term in Eq. (3) is the free energy of the system at the reference state, where μ_i^\ominus is the chemical potential. The second term in Eq. (2) corresponds to the gradient energy density

$$f_{grad}(\eta_k) = \frac{\kappa(\boldsymbol{\eta})}{2} \sum_k (\nabla \eta_k)^2 \quad (5)$$

where $\kappa(\boldsymbol{\eta})$ is the gradient energy coefficient related to the interface surface energy and width of the interface (l). The last term in Eq. (2)

$$f_{elec}(C_i, \varphi) = \rho_e \varphi \quad (6)$$

corresponds to the electrostatic free energy density, where φ is the electrostatic potential and ρ_e is the electric charge density,

$$\rho_e = F \sum z_i C_i \quad (7)$$

where F is Faraday's constant and z_i is the valence of the ionic species.

The net rate (R_{net}) of any chemical reaction is the balance of forward and backward reactions. To ensure the balance of net reaction, R_{net} for an electrochemical system can be expressed as ³⁴

$$R_{\text{net}} = r_0^{\rightarrow} \exp\left(-\left(\mu_{TS}^{\text{ex}} - \mu_1\right)/R_g T\right) - r_0^{\leftarrow} \exp\left(-\left(\mu_{TS}^{\text{ex}} - \mu_2\right)/R_g T\right) \quad (8)$$

where r_0^{\rightarrow} and r_0^{\leftarrow} are the forward and backward reaction constants, respectively. The excess chemical potential at the transition state is given by μ_{TS}^{ex} , while the chemical potentials at the initial and final state are μ_1 and μ_2 , respectively. The equilibrium reaction constants r_0^{\rightarrow} and r_0^{\leftarrow} are equal ($r_0 = r_0^{\rightarrow} = r_0^{\leftarrow}$) for appropriately defined μ ³⁴. Following the work of Chen et al. ³⁵, it is considered that the evolution of phase field variables follow the electrochemical reaction rate (R_{net}). The relation in Eq. (8) can be described in terms of thermodynamic driving force ($\Delta\mu = \mu_2 - \mu_1$) as,

$$\frac{\partial \eta_k}{\partial t} = r_0 \left\{ \exp\left[-\alpha \Delta\mu_k / RT\right] - \exp\left[(1-\alpha) \Delta\mu_k / RT\right] \right\} \quad (9)$$

where k describes the phases (grain, SGB, crystal orientations and electrolyte) and α is the charge transfer coefficient (or symmetry factor) and $\Delta\mu_k$ is the thermodynamic force, given by

$$\Delta\mu_k = \frac{\delta G}{\delta C_k} = nF\psi_k \quad (10)$$

where ψ_k is the total overpotential, which is given by $\psi_k = \psi_{a,k} + \psi_{c,k}$. Here, $\psi_{a,k}$ and $\psi_{c,k}$ represent the activation and concentration overpotential for k , respectively. The normalized concentration c_i of metal atom and ions are normalized by $c_i = C_i / C_{Al,o}$, where $C_{Al,o}$ is the bulk molar concentration of metal in solid phase. Following the same derivation process as detailed in Appendix A of Ansari et al.³³, Eq. (9) takes the form,

$$\frac{\partial \eta_k}{\partial t} = -L_{\text{int}} \left[\frac{\partial f_0}{\partial \eta_k} - \kappa(\boldsymbol{\eta}) \nabla^2 \eta_k \right] - L_r \lambda_k S \left\{ \exp \left[\frac{(1-\alpha)nF\psi_k}{R_g T} \right] - a_{A^{r+3}} \exp \left[\frac{-\alpha nF\psi_k}{R_g T} \right] \right\} \quad (11)$$

$$\eta_{\text{elec}} = 1 - \sum_{i=1}^k \eta_k \quad (12)$$

$$\psi_k = E_{\text{app}} - E_{\text{cor}}^k - \varphi \quad (13)$$

The parameters L_{int} and L_r are phase field model parameters. The activity a_i of an ion is given by $a_i = \zeta_i(c_i)$, where ζ_i is the activity coefficient. The second term on the right side in Eq. (11) is localized at the corroding interface. Therefore, it is necessary to define λ_k in such a way that this reaction is localized at that particular interface. For a two phase PF model, the gradient of the monotonously varying function $-2\eta^3 + 3\eta^2$ localizes the reaction at the interface but a MPF model needs a more generic function to localize such reaction at an interface. Moelans introduced such a monotonous function for a MPF model which is given by³⁶,

$$H_i = \frac{\eta_i^2}{\sum_{j=1}^N \eta_j^2} \quad (14)$$

where N represents all the phase field variables including η_{elec} . This model considers grain, SGBs and grain orientations can be represented by $\boldsymbol{\eta}$, whenever such phase/grain orientation interacts with the electrolyte, the electrochemical reaction is taken into consideration by following relation,

$$\lambda_k = 4H_k H_{elec} \quad (15)$$

The metal ion concentration affects the corrosion rate when it is close to the saturation value. Therefore, a simple relation is used to incorporate this effect by using the variable S given by, $1 - c_{Al^{+3}}/c_{sat(Al^{+3})}$. Corrosion potential E_{cor}^k is a material property and varies with material composition and crystal orientation. Therefore, each grain, crystal orientation and SGB has different corrosion potential values.

IONS CONCENTRATION EVOLUTION

The time-dependent evolution of metal ion (cation) and anions in the electrolyte is given by the Nernst-Planck equation. This equation also incorporates the source sink terms and is expressed as,

$$\frac{\partial c_i}{\partial t} = \nabla D_i^{eff} \nabla c_i + \nabla \frac{z_i D_i^{eff} F c_i}{R_g T} \nabla \phi + R_i \quad (16)$$

where i represents the ionic species of the electrolyte. The diffusion coefficient varies from one phase to another. Therefore, it is expressed as a function of phase fractions and is given by,

$$D_i^{eff} = \sum_{j=1} D_i^j H_j \quad (17)$$

where D_i^j is the diffusion coefficient of ionic specie i in phase j . R_i is the term related to the consumption or production of ions in the electrolyte as a result of electrochemical reactions.

The electrostatic potential in the electrolyte is given by,

$$\nabla[\sigma_e \nabla \phi] = I_r \quad (18)$$

where σ_e is the electronic conductivity in the electrolyte. I_r is the current density and is related to the reaction rate of Eq. 11 and is given by,

$$I_r = nFC_{Al,o} \sum_{k=1}^N \frac{\partial \eta_k}{\partial t} \quad (19)$$

where n is the number of electrons produced or absorbed as a result of reaction (1). $C_{Al,o}$ is the molar concentration of aluminum in the bulk phase.

NUMERICAL IMPLEMENTATION

Fig 2 shows the 2-D geometry of sensitized metal with grain and SGBs. The SGB has a finite width (w_{sgb}) and its value is chosen based on the interface thickness of phase field variables. In this work, the interface thickness is considered to be five times smaller than SGB width ($w_{sgb} = 5l$). A smaller interface thickness requires smaller mesh elements to discretize the geometry. Therefore, the interface thickness can be reduced further at the expense of computational cost. The interface thickness value is given for each simulation case in the Results and Discussion section.

The PF model parameters m and $\kappa(\eta)$ are related to surface energy or surface tension σ_k and interface thickness l . Surface tension on each evolving interface can be different, which should result in a different PF parameter $\kappa(\eta)$. Kazaryan et al. proposed a relation for $\kappa(\eta)$ as a function of surface tension³⁷. Although it is possible to employ this proposed relation in our work but, for the sake of simplicity, it is considered as constant. κ and m for all the binary interfaces are given by, $m = 6\sigma/l$ and $\kappa = (3/4)\sigma l$ for all $\gamma_{i,j}=1.5$ ³⁶. ζ_i is the activity coefficient of the ionic specie and is equal to 1 in all simulations. It should be noted that the grain orientation effect was not included in any of the examples reported in this work. It was ignored due to the absence of such data (corrosion rate dependence on grain orientation, which is usually obtained by orientation image microscopy) in the reference experimental studies used for comparison but it can be easily studied using this MPF model, as reported in one of our earlier work³².

The proposed MPF for IGC is applied for 2-D and 3-D geometries. The boundary conditions for 2-D geometry are given in Fig 3. The boundary conditions in the 3-D case are the same as given for the 2-D case. The only difference is that each boundary in the 2-D geometry represents a surface in 3-D. The initial values in grain phase (grey) are $\eta_g=1$, $\eta_{GB}=\eta_{elec}=0$, $c_i=0$ and $\varphi=0$. The initial values in the SGB phase (black) are $\eta_{GB}=1$, $\eta_g=\eta_{elec}=0$, $c_i=0$ and $\varphi=0$. Similarly, the initial values in the electrolyte phase (blue) are $\eta_g=\eta_{GB}=0$, $\eta_{elec}=1$, $c_i=c_{i,o}$ (given in Table 1) and $\varphi=0$. The governing Eqs. (11), (12), (16) and (18) are solved by the finite element method. The standard Galerkin³⁸ formulation is used to discretize the space, and the backward differentiation formula (BDF) method³⁹, due to its inherent stability, is used for the time integration of the governing equations. Triangular and tetrahedral Lagrangian mesh elements are used to discretize the 2-D and 3-D geometries, respectively.

RESULTS AND DISCUSSION

In this section, the MPF model for IGC is validated against different experimental findings available in the literature on aluminum alloys. IGC depends on electrochemical exposure time, applied potential, degree of sensitization and plane-direction in rolled sheets. Several studies are performed to validate the simulation results with the experimental findings and discussions are made with the underlying factors in detail.

EFFECT OF ELECTROCHEMICAL EXPOSURE

First case is focused on the IGC corrosion rate comparison with a thin 2-D foil of AA2024⁷. The scanning electron microscope (SEM) images of the experimental findings are shown in Fig 4(a). The microstructure shown in Fig 4(b) is sketched/ drawn as geometry file in COMSOL Multiphysics. Although β -phase thickness can be considered equal to or less than 0.1 μm as reported in literature⁴, it comes at the expense of computation cost. The computation cost increases with the decrease in the interface width (l_i) for all phase field variables, assuming the size of the geometry remains unchanged. In this case, l_i for all the phases is considered equal to 2 μm (corresponds to a SGB width of 10 μm). Please note, β -phase thickness is usually not uniform in the entire sample but for the sake of simplicity, it is considered uniform. This 2-D model geometry is exposed to a 0.1M NaCl solution at an applied potential of -0.6 V_{SCE} (V_{SCE} = volts versus saturated calomel electrode), as reported in the reference experiment⁷. This applied potential is slightly higher than the OCP. The corrosion potential of β -phase in Al alloys is reported to be equal to -0.92 V_{SCE} ⁴. The corrosion potential for the grain is considered equal to -0.75 V_{SCE} . This value is assumed to be higher than the corrosion potential of β -phase but lower than the applied potential.

MPF model simulations show good agreement with the experimental results quantitatively, as shown in Fig 4(c). The IGC depth for both simulated MPF and experimental results versus time have a non-linear relation with time, as shown in Fig 5. The results are also compared with the Peridynamic (PD) model²⁵, as shown in Fig 5. It can be seen that PD model tends to overestimate the IGC rate at the start as compared to the experimental and

MPF model results. This is probably due to the approximation made in the PD model that the process becomes diffusion controlled right away²⁵. Experimental and MPF model results show that the IGC depth has a non-linear relation suggesting that the process is transport controlled. Further analysis showed that the metal ion concentration is still lower than the saturation value at the corroding surface, as shown in Fig 6(a). It means that the process is still not diffusion controlled. The electric potential distribution in the electrolyte does have a higher value near the corroding surface, as shown in Fig 6(b). This high value of electrostatic potential corresponds to the non-linear IGC rate making the process migration controlled. The IGC mechanism resembles with crevice corrosion. In this case, the apparent crevice (corroded SGB) width is only a few microns while the depth is hundreds of microns. The slow movement of metal ions through thin electrolyte film (hindrance by high electrostatic potential and metal ion saturation in the nearby electrolyte) in the corroded sensitized SGBs makes the process migration controlled.

It should be noted that the size of grain and SGB in the previous simulation was scaled up to reduce the computation cost while comparing the computational results on an engineering scale. In order to reduce the influence of this scaling, the grain size was kept significantly higher than the width of SGB (w_{sgb}). Now another set of simulations is performed where the w_{sgb} is considered to be $2\mu\text{m}$, which is closer to the IGC width reported in the literature. It is important to note that the simulations are performed for the same conditions as reported earlier and simulated results are shown in Fig 7. A comparison is drawn between the simulation and experimental results. It can be seen that the simulation results are very much in the same range as the experimental results. The difference lies in the non-uniform nature of corrosion in the experimental results which is uniform in the

MPF simulations. This is due to the assumption of uniformly distributed SGB in the simulations.

IGC IN HEAT-TREATED ROLLED ALUMINUM SHEETS

Al alloys show different penetration rate in different directions of rolled sheets. Here an experimental study ⁴ is chosen to validate IGC by MPF model. A 2-D model is simulated with experimental conditions taken from the experimental study ⁴. The experimental study reported the experiments performed on a heat treated Al-Mg alloy (AA5XXX). Several samples were prepared for heat treatment with different conditions. Barker's etch images revealed that samples with lower DOS values have less sensitized GBs ⁴. Therefore, heat treated sample with the highest DOS value 49 mg/cm² (30 days at 100 °C) is considered for simulation with 2-D MPF model with an assumption that all the SGBs are uniformly sensitized. The simulation conditions taken from the experiments for this study are applied potential (-0.73 V_{SCE}) and 0.6 M NaCl solution ⁴. The corrosion potential for β -phase is taken as -0.92 V_{SCE} ⁴. The interface width of the phase field variables is taken equal to 5 μ m. The average grain size along different plane directions reported in the experimental study are longitudinal direction (L)=80 μ m, long transverse direction (T)= 60 μ m and short transverse direction (S)= 20 μ m ⁴. These grain size dimensions are scaled up by a factor of three to make sure that the grain size is significantly larger than the β -phase. In this first study, the sample is exposed at the S-T surface and damage morphology is observed in the L direction. The optical images of the experimental results are shown in Fig 8(a). Please note the difference in length scale of the experimental results at different time intervals.

The MPF model results have wider corroded grain and SGB as compared to the experimental results. The difference in morphology of MPF model results and optical images is due to the assumption that the SGB is uniformly sensitized and also its width which is quite small in the experimental case. The IGC depth predicted by MPF model results quantitatively agrees well with the experimental results, as shown in Fig 9.

This comparison also includes a plot proposed by linear relation approximation made by the statistical model based on these experimental results ⁴. This model predicts that for DOS value of 49 mg/cm², the IGC rate can be approximated by the linear relation 2.64 ± 0.80 (nm/s) ⁴. The linear relation prediction agrees with the MPF models except for a small deviation at a later stage. The MPF model predicts that the process will go through a transition from being reaction-controlled to transport-controlled after 50 hours of electrochemical exposure. The metal ion concentration at the corroding surface is significantly lower than the saturation value, as shown in Fig 10(a). Therefore, the process is far from being diffusion controlled. However, the electrostatic potential is small but not negligible. The slightly non-linear trend after 50 hours is most probably due to the process being migration controlled. This can also be observed from Fig 10(b), where the electric potential at the corroding surface is around 1mV after 24 hours of electrochemical exposure. This value increases with time and reaches around 5 mV at the corroding surface after 72 hours.

EFFECT OF PLANE-DIRECTION ON IGC IN HEAT TREATED ROLLED ALUMINUM SHEETS

In order to investigate the effect of rolling-direction on IGC rate, more simulations are performed. The MPF model simulations are performed based on the heat treated rolled Al-Mg alloy (AA5XXX) ⁴. The samples are rolled in L-direction and hence have different grain size in three plane-directions. Please note, this experiment is the same as discussed and used for comparison in the previous case. Therefore, experimental conditions and model parameters are the same as reported in the previous case.

In this case, the LT surface of the metal is exposed to the electrolyte to observe IGC in the S-direction. The grain size along the S-direction is three times smaller than the T-direction. MPF model results of IGC evolution for both L- and S-direction are shown in Fig 11(a) and (b), respectively. The results show that the IGC is slower in S-direction as compared to the L- direction. The experimental results also report lower IGC rate along S-direction ⁴. The difference in IGC along the L- and S-directions is solely due to the difference in the microstructure (average grain size along the corroding direction) of these two directions.

3-D SIMULATIONS OF MPF MODEL FOR IGC

Metals have complex microstructure and can have non-uniform material properties in a single component. The localized corrosion of a metal depends on the geometry and the change in corroding morphology can have significant effect on the corrosion rate. In all the cases presented in this work, comparisons with the experimental results are made for sensitized thin sheets experiments. These experiments were intentionally performed for thin sheets to reduce the effect of microstructure in the third dimension and understand the IGC kinetics in general. But in real life, corrosion of metallic structures mostly happens in 3D. It would be more reasonable to predict the corrosion kinetics of such an industrial problem with a 3-D geometry.

Here, we study the IGC kinetics of sensitized metal in an electrolyte in 3-D using the MPF model. It is possible to assign each grain a different grain orientation, as done in our previous works^{27,33}. This study assumes that the effect of individual grain orientation is negligible as compared to the difference in grains and SGBs. It is also possible to incorporate the effect of plane-direction dependence, as presented for the 2-D cases. For the sake of simplicity, it is considered that the metal is not mechanically rolled and hence, the grain size along all plane directions is similar. The geometry of the problem under consideration is shown in Fig 12(a). To better visualize grain and SGBs geometry at the corroding surface, the electrolyte phase is hidden in Fig 12(b). The evolution of sensitized Al-Mg alloy is studied in a 0.1 M NaCl solution at an applied potential of $-0.7 V_{SCE}$. The corrosion potential along the β -phase is equal to $-0.92 V_{SCE}$, taken from literature⁴. The applied potential is also slightly higher than the corrosion potential of grains ($-0.75 V_{SCE}$),

which makes the grains anodic as well. The interface thickness for all the phases is assumed to be 5 μm . The MPF results show that SGBs corrode at higher rate as compared to grains. The evolution of all three phases, grain, SGBs and electrolyte is shown in Fig 12(a) at 250 s, 500 s and 1000 s in a transparent mode. The same evolution is shown in Fig 12(b), where electrolyte phase is hidden to better visualize the evolving grain and SGB phases. This study shows that this MPF is equally capable of solving complex 3-D geometry problems.

CONCLUSIONS

In this work, a multi-phase-field (MPF) model was proposed to study the intergranular corrosion (IGC) kinetics of sensitized metallic materials in corrosive electrolytes.

The proposed MPF model was used to study the effect of electrochemical exposure on an aluminum alloy (AA2024) in NaCl solution. IGC rate and morphology of the simulated results showed reasonable agreement with the well-established experimental results. The simulation results also showed that the corrosion rate was significantly higher along the sensitized grain boundaries (SGBs) where almost no corrosion was observed in the grains. The grains were in fact anodic in the model (unlike majority of the previous modeling studies that assume them non-corrodible), but the grains corrode at a much lower rate as compared to SGBs due to the difference in the material properties of metal in the grain and SGB phases. The simulation results also showed that the corrosion rate along SGB decreases with time due to the slow transport of metal ions in the electrolyte through the narrow corroded SGB regions. The MPF model was also employed to study IGC corrosion kinetics of rolled aluminum sheets (AA5XXX) in NaCl solution. The

simulation results of this study showed good agreement with the experimental results, quantitatively. The model was also able to show the effect of rolling plane-direction on IGC kinetics, which agreed well with the experimental results, qualitatively. As the results and discussion section showed, the MPF model can easily solve the IGC problems for 3-D geometries.

ACKNOWLEDGEMENT

This work was supported by Research Grants Council of Hong Kong (PolyU 152140/14E and PolyU 152174/17E) and funds from the Hong Kong Polytechnic University (1-99QP, RUTS and 4-88Y2).

Competing Interests

The authors declare no competing interests.

Author Contribution

T.Q.A and S.Q.S conceived the idea. T.Q.A developed the model, performed simulations and wrote the manuscript. S.Q.S and J-L.L provided critical comments and contributed to revisions of the manuscript.

REFERENCES

1. W. Zhang and G. Frankel, *Journal of the Electrochemical Society*, **149** (11), B510-B519 (2002).
2. E. Akiyama and G. Frankel, *Journal of The Electrochemical Society*, **146** (11), 4095-4100 (1999).
3. S. Jain, J. Hudson, and J. Scully, *Electrochimica Acta*, **108** 253-264 (2013).
4. M. Lim, J. Scully, and R. Kelly, *Corrosion*, **69** (1), 35-47 (2013).
5. C. Luo, X. Zhou, G. Thompson, and A. Hughes, *Corrosion Science*, **61** 35-44 (2012).
6. X. Zhou, C. Luo, Y. Ma, T. Hashimoto, G. Thompson, A. Hughes, and P. Skeldon, *Surface and Interface analysis*, **45** (10), 1543-1547 (2013).
7. R. Bonzom and R. Oltra, *Corrosion Science*, **111** 850-855 (2016).
8. W. Zhang and G. Frankel, *Electrochimica Acta*, **48** (9), 1193-1210 (2003).
9. X. Zhang, X. Zhou, T. Hashimoto, and B. Liu, *Materials Characterization*, **130** 230-236 (2017).
10. X. Zhang, X. Zhou, T. Hashimoto, J. Lindsay, O. Ciuca, C. Luo, Z. Sun, and Z. Tang, *Corrosion Science*, **116** 14-21 (2017).
11. S. Jain, M. Lim, J. Hudson, and J. Scully, *Corrosion Science*, **59** 136-147 (2012).
12. S. Knight, M. Salagaras, and A. Trueman, *Corrosion Science*, **53** (2), 727-734 (2011).
13. N. N. Aung and W. Zhou, *Corrosion Science*, **52** (2), 589-594 (2010).
14. W. Zhou, T. Shen, and N. N. Aung, *Corrosion Science*, **52** (3), 1035-1041 (2010).
15. W. Song, H. J. Martin, A. Hicks, D. Seely, C. A. Walton, W. B. Lawrimore II, P. T. Wang, and M. Horstemeyer, *Corrosion Science*, **78** 353-368 (2014).
16. C. Tedmon, D. Vermilyea, and J. Rosolowski, *journal of the Electrochemical Society*, **118** (2), 192-202 (1971).
17. E. L. Hall and C. L. Briant, *Metallurgical Transactions A*, **15** (5), 793-811 (1984).
18. B. W. Bennett and H. W. Pickering, *Metallurgical Transactions A*, **18** (6), 1117-1124 (1991).
19. W. Zhang, S. Ruan, D. Wolfe, and G. Frankel, *Corrosion Science*, **45** (2), 353-370 (2003).
20. M. L. C. Lim, R. Matthews, M. Oja, R. Tryon, R. G. Kelly, and J. R. Scully, *Materials & Design*, **96** 131-142 (2016).

21. D. Mizuno and R. Kelly, *Corrosion*, **69** (7), 681-692 (2013).
22. D. Mizuno and R. Kelly, *Corrosion*, **69** (6), 580-592 (2013).
23. S. Lishchuk, R. Akid, K. Worden, and J. Michalski, *Corrosion Science*, **53** (8), 2518-2526 (2011).
24. D. Di Caprio, J. Stafiej, G. Luciano, and L. Arurault, *Corrosion Science*, **112** 438-450 (2016).
25. S. Jafarzadeh, Z. Chen, and F. Bobaru, *Journal of The Electrochemical Society*, **165** (7), C362-C374 (2018).
26. W. Mai, S. Soghrati, and R. G. Buchheit, *Corrosion Science*, **110** 157-166 (2016).
27. T. Q. Ansari, Z. Xiao, S. Hu, Y. Li, J.-L. Luo, and S.-Q. Shi, *npj Computational Materials*, **4** (1), 38 (2018).
28. A. F. Chadwick, J. A. Stewart, R. A. Enrique, S. Du, and K. Thornton, *Journal of The Electrochemical Society*, **165** (10), C633-C646 (2018).
29. P. Stähle and E. Hansen, *Engineering Failure Analysis*, **47** 241-251 (2015).
30. W. Mai and S. Soghrati, *Corrosion Science*, **125** (Supplement C), 87-98 (2017).
31. C. Lin, H. Ruan, and S.-Q. Shi, *Electrochimica Acta*, **310** 240-255 (2019).
32. T. Q. Ansari and S.-Q. Shi, in "Meeting Abstracts", p. 992-992. The Electrochemical Society, 2019.
33. T. Q. Ansari, J.-L. Luo, and S.-Q. Shi, *npj Materials Degradation*, **3** (1), 28 (2019).
34. M. Z. Bazant, *Accounts of chemical research*, **46** (5), 1144-1160 (2013).
35. L. Chen, H. W. Zhang, L. Y. Liang, Z. Liu, Y. Qi, P. Lu, J. Chen, and L.-Q. Chen, *Journal of Power Sources*, **300** 376-385 (2015).
36. N. Moelans, *Acta Materialia*, **59** (3), 1077-1086 (2011).
37. A. Kazaryan, Y. Wang, S. Dregia, and B. R. Patton, *Physical Review B*, **61** (21), 14275 (2000).
38. G. Fairweather, *Finite element Galerkin methods for differential equations*, M. Dekker, New York, (1978).
39. U. M. Ascher and L. R. Petzold, *Computer methods for ordinary differential equations and differential-algebraic equations*, Siam (1998).
40. R. E. Melchers and R. Jeffrey, *Corrosion Science*, **47** (7), 1678-1693 (2005).

Table 1: Parameters used to numerically solve this MPF models.

Symbol	Description	Value	Source
T	absolute temperature	293K	
R_g	gas constant	8.3145 J/(mol·K)	
F	Faraday constant	96485C/mol	
σ	interface energy	0.5 J/m ²	
l	interface width	2 or 5 × 10 ⁻⁶ m	
L_{int}	kinetic interface parameter	1 × 10 ⁻⁸ m ³ /J s	
$L_{r\Box\Box}$	phase field constant related to metal corrosion	2 × 10 ⁻⁸ 1/s	
E_{cor}^{SGB}	corrosion potential in sensitized GB	-0.92 mV _{SCE}	4
$C_{Al,o}$	molarity of aluminum metal (solid)	100 mol/L	
C_{sat}	saturation molarity of Al^{+3} in electrolyte	3.1 mol/L	
$C_{Al+3,o}$	initial molarity of Fe^{+2} ion in the electrolyte	0	
$C_{Cl-,o}$	initial molarity of Cl^- in the electrolyte	0.60 mol/L and 0.1 mol/L	4 and 7
D_i^m	diffusion coefficient of all ions in the metal phase	0 m ² /s	
D_i^e	diffusion coefficient of all ions in the electrolyte phase	5.53 × 10 ⁻¹⁰ m ² /s	25
σ^e	electrolyte conductivity	4.7 S/m	40
α	charge transfer coefficient	0.5	

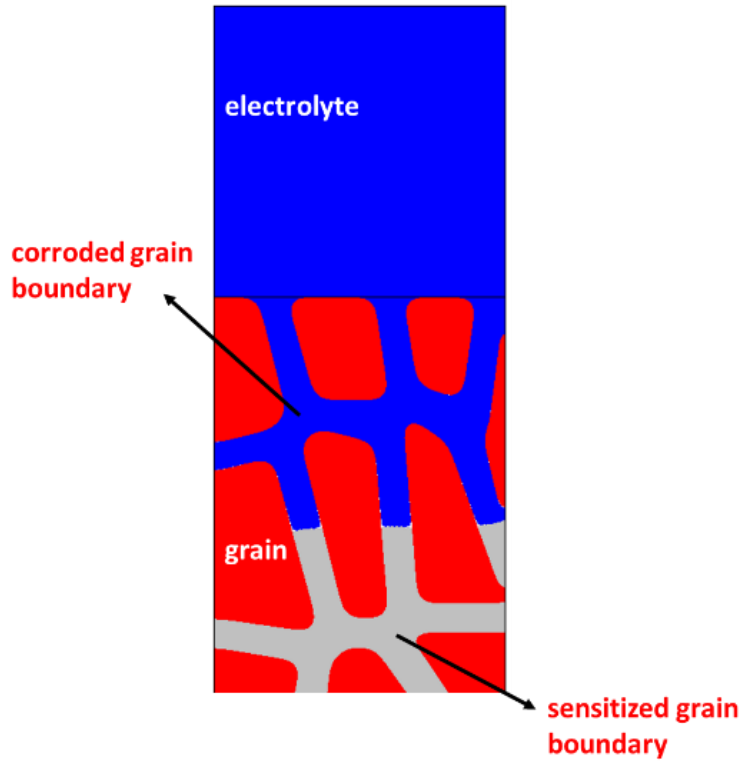


Figure 1: Schematic of intergranular corrosion in a corrosive electrolyte.

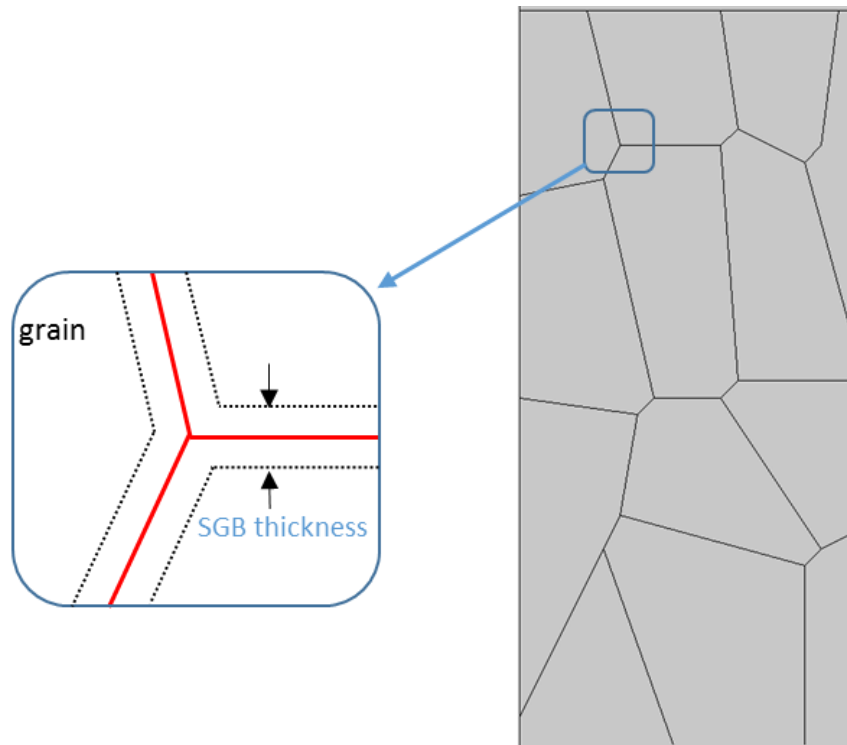


Figure 2: The geometry of the model with grain and sensitized SGB.

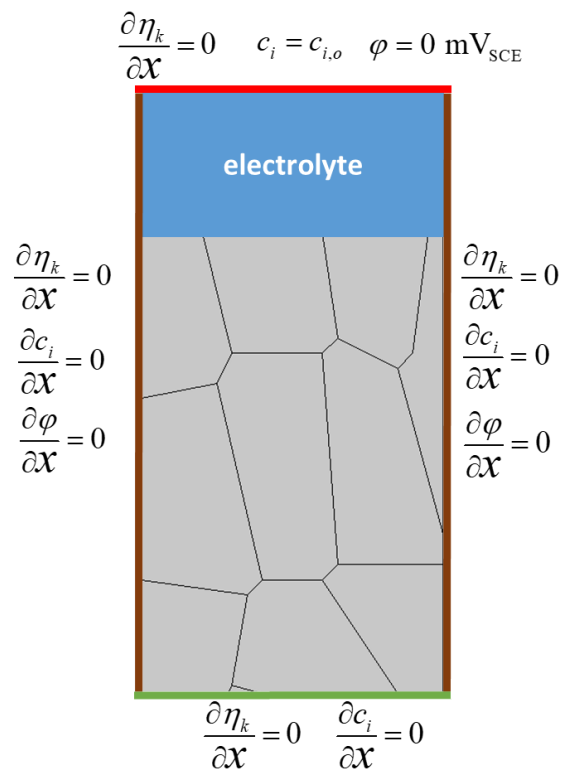


Figure 3: Boundary values for the numerical implementation of this problem.

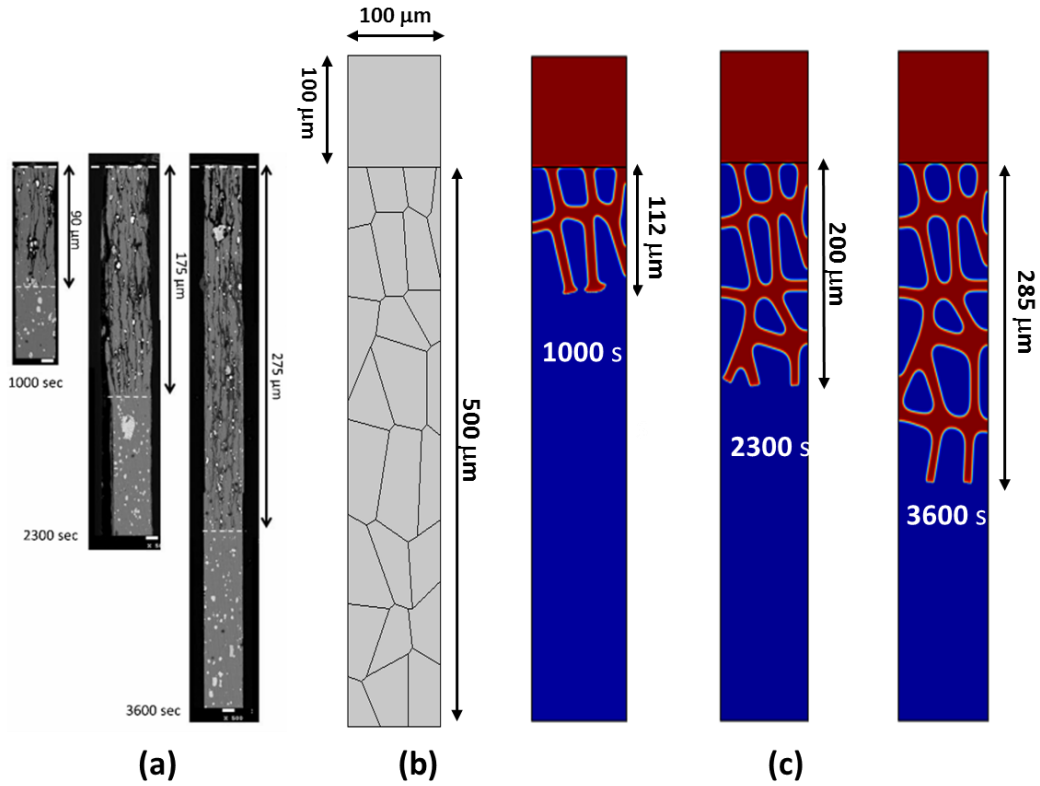


Figure 4: IGC in Al alloy at an applied potential of $-0.6 V_{\text{SCE}}$ in a 0.1 M NaCl electrolyte. (a) Scanning Electron Microscope (SEM) images of experimental findings, taken from literature (reproduced with permission)⁷. (b) The geometry of the microstructure used in the simulations. (c) MPF model results for the evolution of $\eta_{\text{electrolyte}}$ with time (electrolyte phase= red color and un-corroded metal= blue).

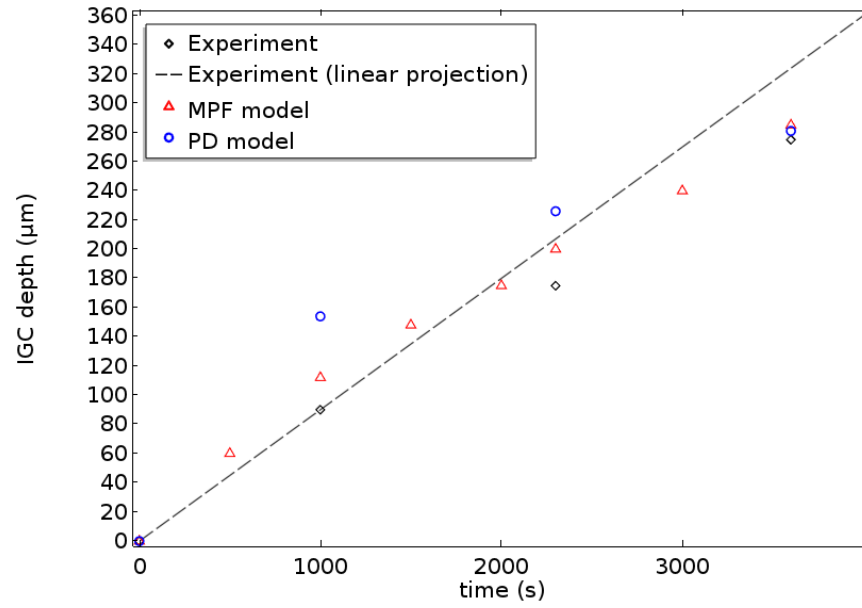


Figure 5: Comparison of IGC depth versus time between MPF model, PD model²⁵ and experiment results⁷.

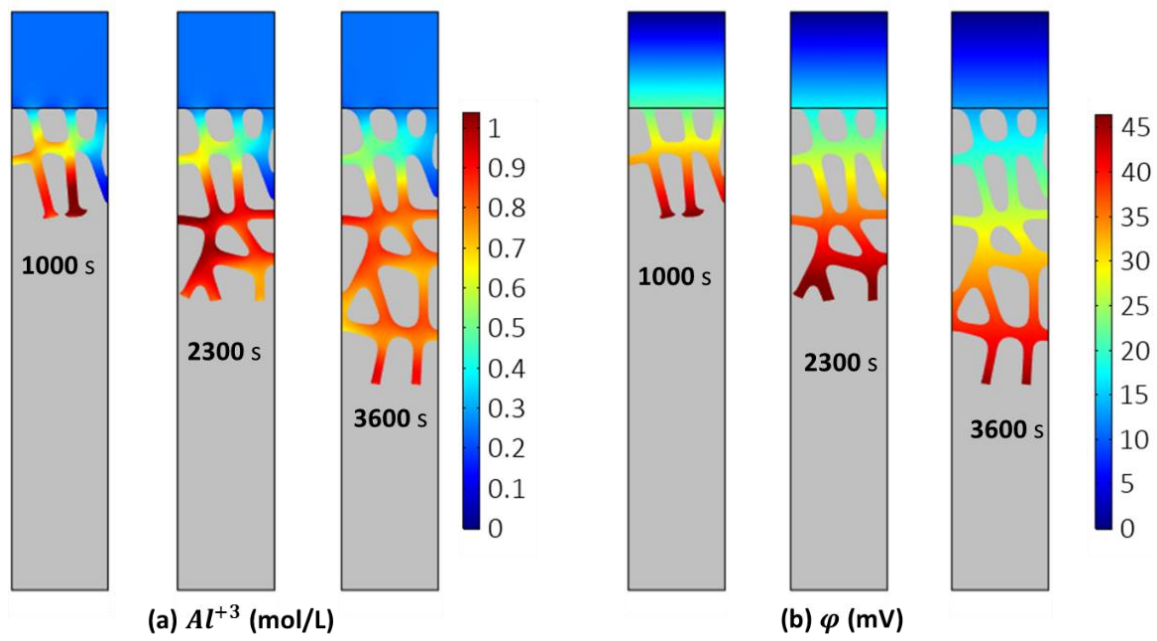


Figure 6: IGC in Al alloy at an applied potential of $-0.6 V_{SCE}$ in a 0.1 M NaCl electrolyte. The evolution of (a) Metal ion (Al^{+3}) (mol/L) and (b) electric potential (mV) distribution.

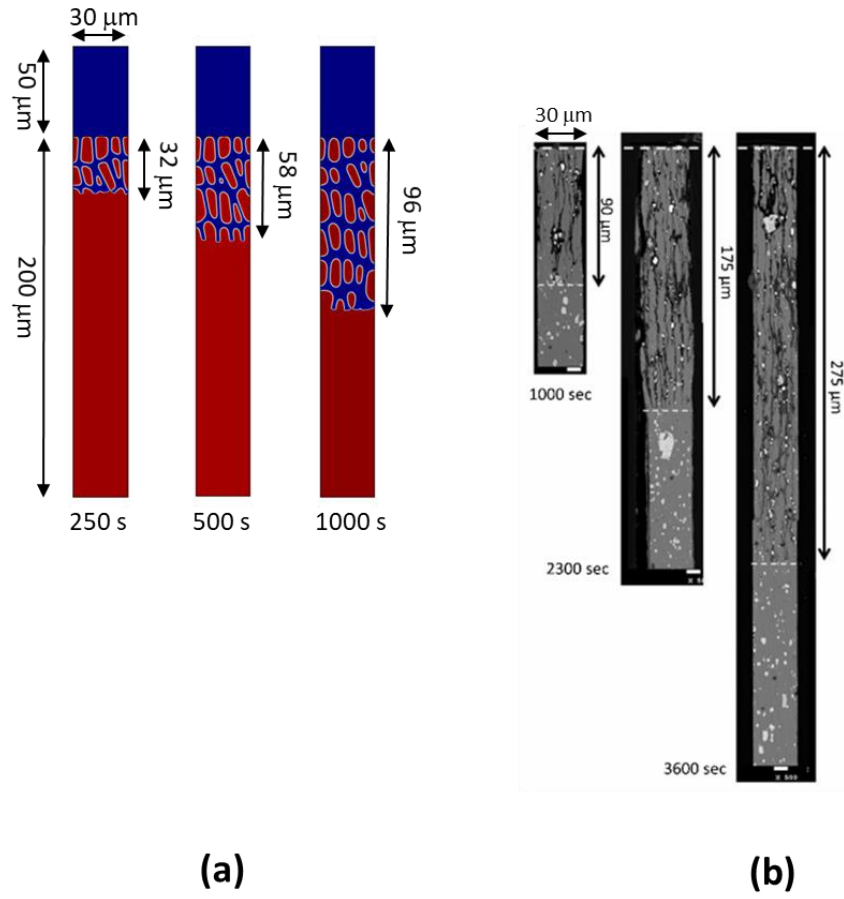


Figure 7: Comparison of (a) MPF model simulations with smaller SGB width and (b) experimental SEM images for IGC (reproduced with permission)⁷.

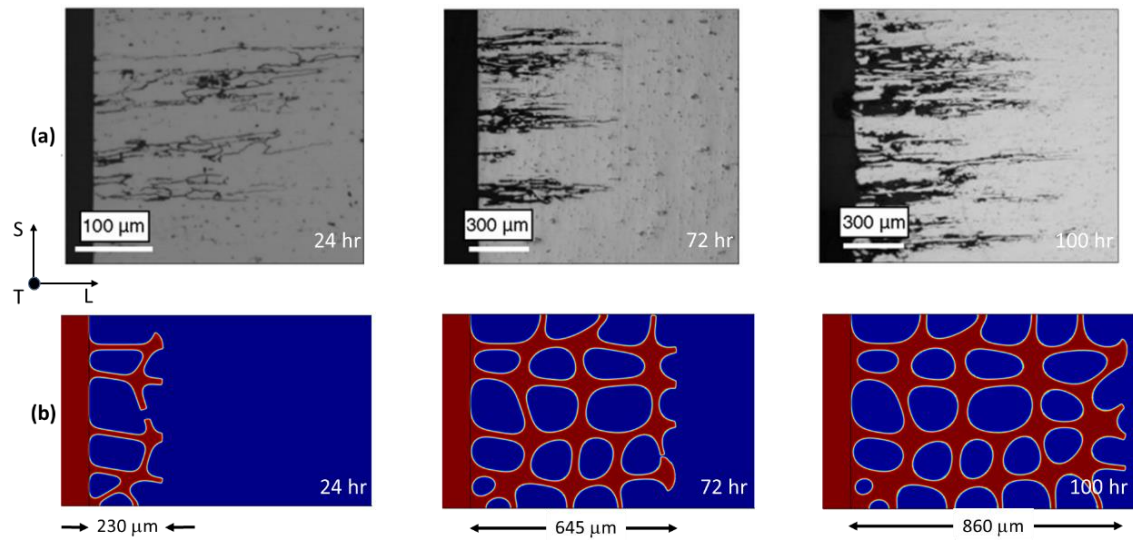


Figure 8: ST surface of the metal exposed to 0.6M NaCl solution at an applied potential of $-0.73 V_{SCE}$. The damage is observed in L-direction where (a) shows the SEM images of the damaged SL surface, taken from the literature (reproduced with permission)⁴, similarly (b) shows the MPF model results where red color is for the electrolyte phase and blue color for metal phase (both grain matrix and β -phase).

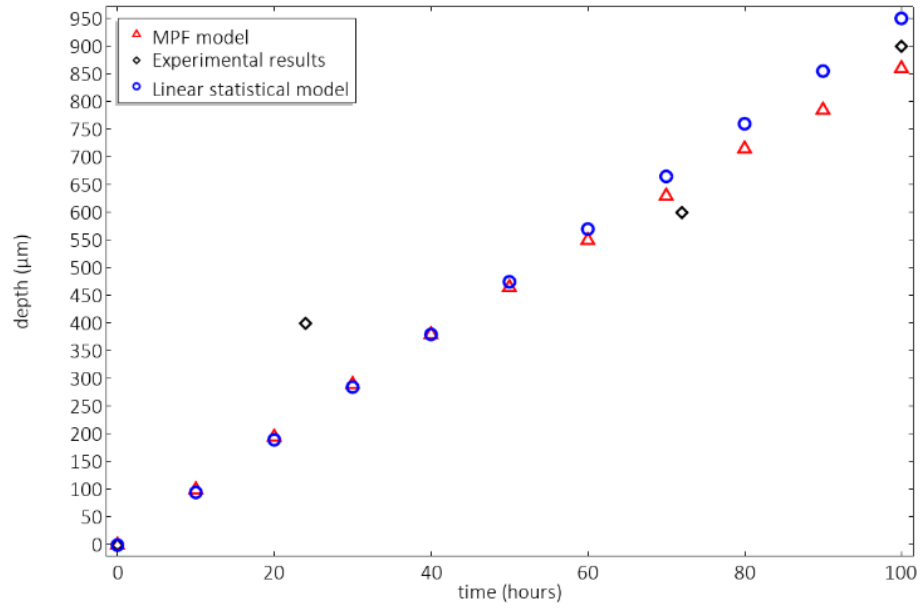


Figure 9: IGC depth versus time for MPF model, experimental⁴ and linear statistical model⁴ results.

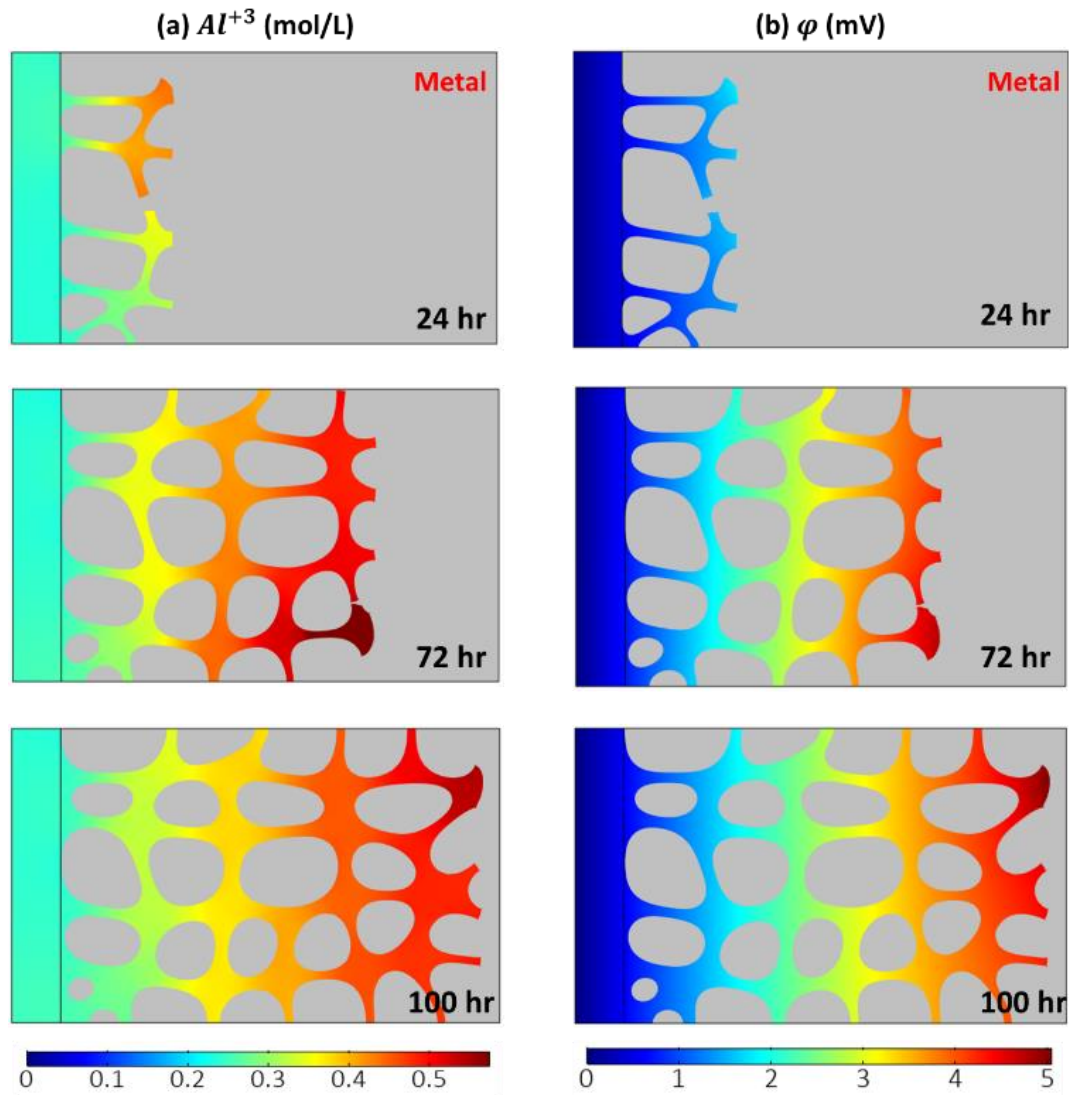


Figure 10: ST surface of the metal exposed to 0.6M NaCl solution at an applied potential of $-0.73 V_{SCE}$. The evolution of (a) Metal ion (Al^{+3}) (mol/L) and (b) electric potential distribution with time. Note: gray color shows the metal phase.

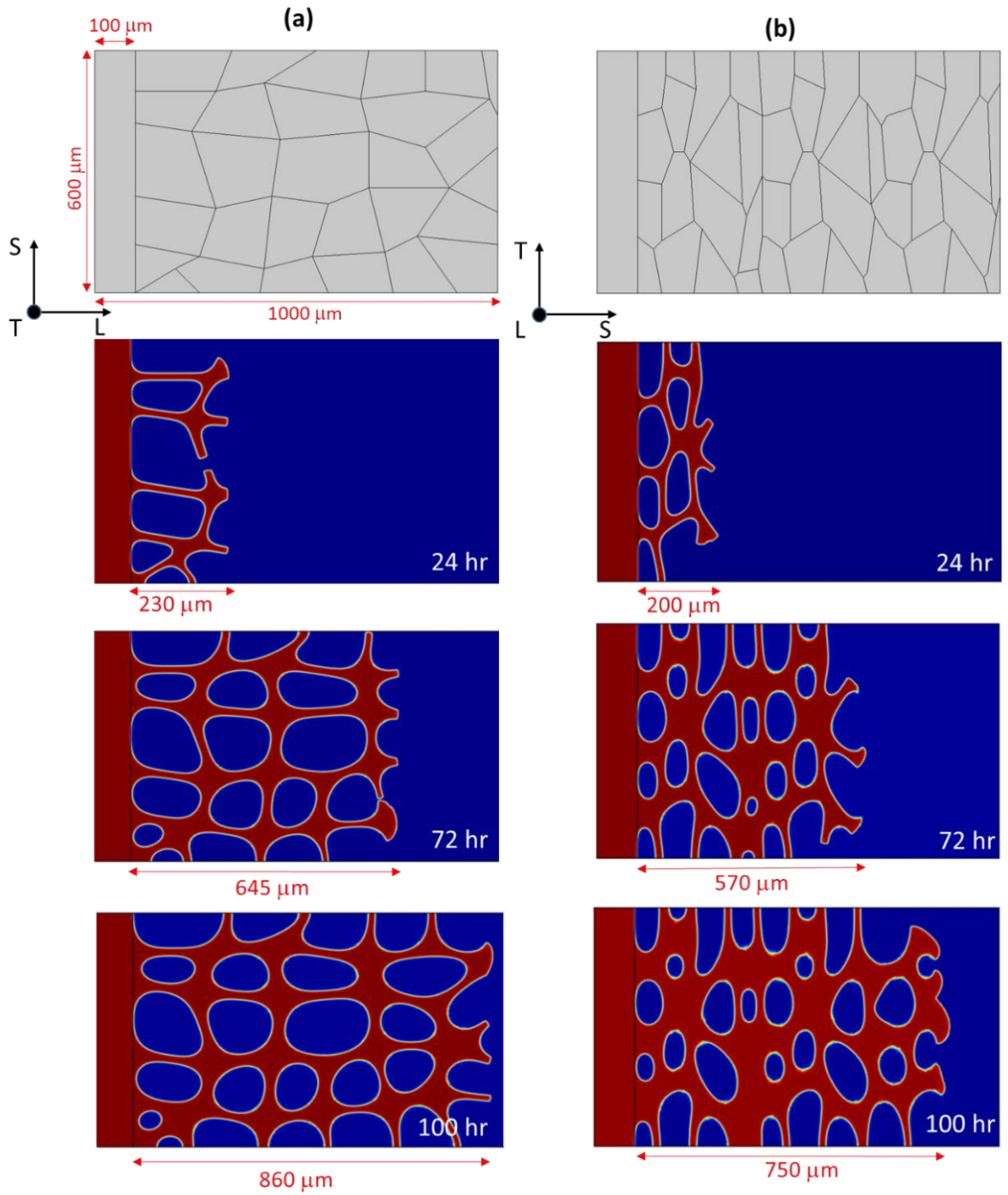


Figure 11: MPF model results for metal corrosion exposed to a 0.6 M NaCl solution from left side at an applied potential of $-0.73 \text{ V}_{\text{SCE}}$. (a) shows the damage evolution in L-direction when exposed from ST surface while (b) shows the damage evolution in S-direction when exposed from LT surface.

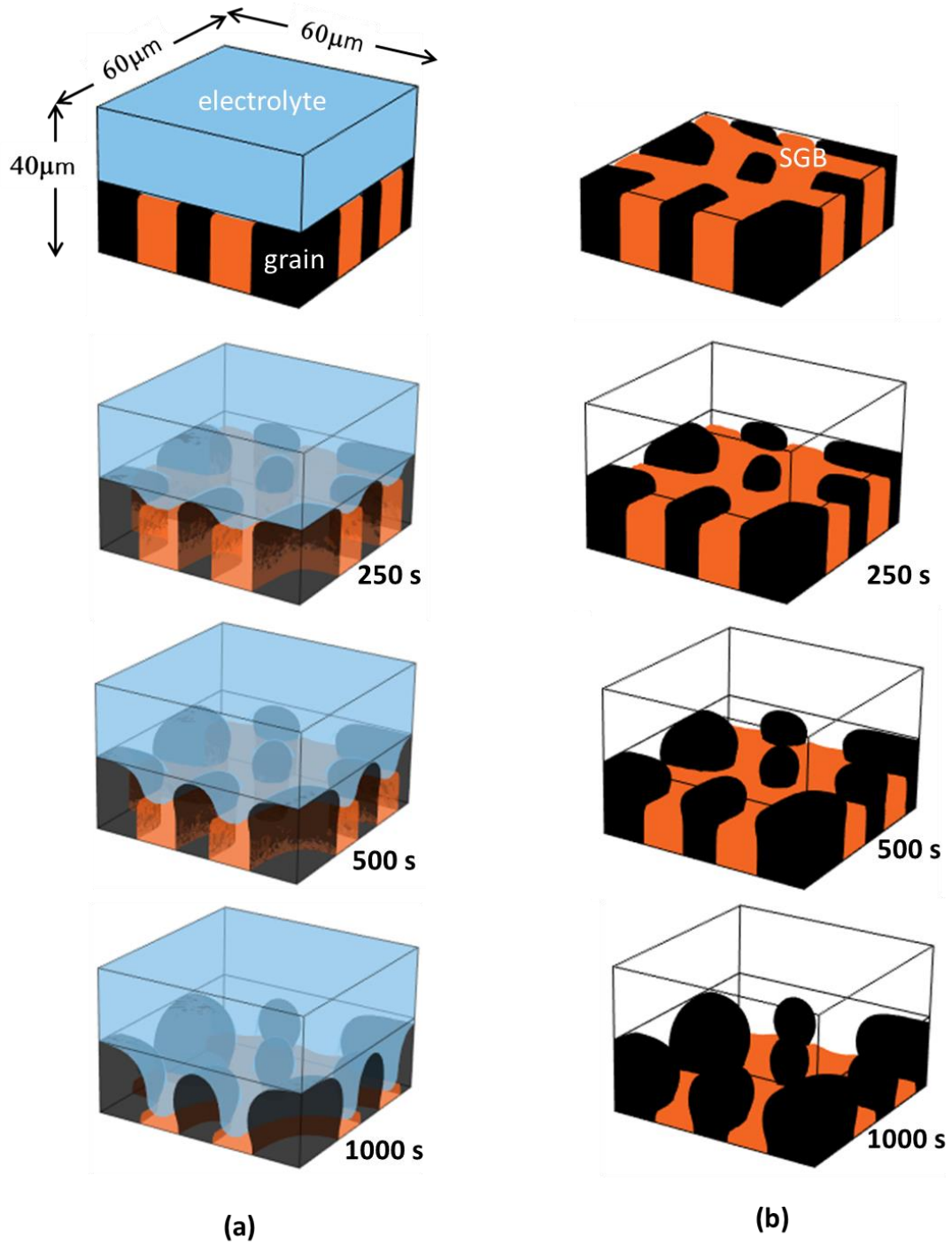


Figure 12: MPF model simulations for a 3-D geometry at an applied potential of $-0.7 V_{SCE}$. Top left one shows the geometric dimensions of the problem under study, while top right shows the geometry where electrolyte phase is hidden. (a) shows the evolution of all three phases (η_{grain} , η_{GB} and $\eta_{\text{electrolyte}}$) over time. (b) shows the evolution of grain and GB (η_{grain} and η_{GB}) over time.